

# Northumbria Research Link

Citation: Kathayat, Gayatri, Sinha, Ashish, Breitenbach, Sebastian, Tan, Liangcheng, Spötl, Christoph, Li, Hanying, Dong, Xiyu, Zhang, Haiwei, Ning, Youfeng, Allan, Robert J., Damodaran, Vinita, Edwards, R. Lawrence and Cheng, Hai (2022) Protracted Indian monsoon droughts of the past millennium and their societal impacts. Proceedings of the National Academy of Sciences of the United States of America, 119 (39). e2207487119. ISSN 0027-8424

Published by: National Academy of Sciences

URL: <https://doi.org/10.1073/pnas.2207487119>  
<<https://doi.org/10.1073/pnas.2207487119>>

This version was downloaded from Northumbria Research Link:  
<https://nrl.northumbria.ac.uk/id/eprint/50489/>

Northumbria University has developed Northumbria Research Link (NRL) to enable users to access the University's research output. Copyright © and moral rights for items on NRL are retained by the individual author(s) and/or other copyright owners. Single copies of full items can be reproduced, displayed or performed, and given to third parties in any format or medium for personal research or study, educational, or not-for-profit purposes without prior permission or charge, provided the authors, title and full bibliographic details are given, as well as a hyperlink and/or URL to the original metadata page. The content must not be changed in any way. Full items must not be sold commercially in any format or medium without formal permission of the copyright holder. The full policy is available online: <http://nrl.northumbria.ac.uk/policies.html>

This document may differ from the final, published version of the research and has been made available online in accordance with publisher policies. To read and/or cite from the published version of the research, please visit the publisher's website (a subscription may be required.)

1  
2  
3  
4  
5  
6  
7  
8  
9  
10  
11  
12  
13  
14  
15  
16  
17  
18  
19  
20  
21  
22  
23  
24  
25  
26  
27  
28  
29  
30  
31  
32  
33  
34  
35  
36  
37  
38  
39  
40  
41  
42  
43  
44  
45  
46  
47  
48

## Protracted Indian Monsoon Droughts of the Past Millennium and Their Societal Impacts

Gayatri Kathayat<sup>a,1</sup>, Ashish Sinha<sup>b,1</sup>, Sebastian F.M. Breitenbach<sup>c</sup>, Liangcheng Tan<sup>d</sup>, Christoph Spötl<sup>c</sup>, Hanying Li<sup>a</sup>, Xiyu Dong<sup>a</sup>, Haiwei Zhang<sup>a</sup>, Youfeng Ning<sup>a</sup>, Robert J Allan<sup>f</sup>, Vinita Damodaran<sup>g</sup>, R. Lawrence Edwards<sup>h</sup>, and Hai Cheng<sup>a,d,i,1</sup>

<sup>a</sup>Institute of Global Environmental Change, Xi'an Jiaotong University, Xi'an 710054, China.

<sup>b</sup>Department of Earth Science, California State University Dominguez Hills, Carson, CA 90747, USA.

<sup>c</sup>Department of Geography and Environmental Sciences, Northumbria University, UK

<sup>d</sup>State Key Laboratory of Loess and Quaternary Geology, Institute of Earth Environment, Chinese Academy of Sciences, Xi'an 710061, China.

<sup>e</sup>Institute of Geology, University of Innsbruck, Innsbruck 6020, Austria.

<sup>f</sup>Climate Monitoring and Attribution Group, Met Office Hadley Centre, UK.

<sup>g</sup>University of Sussex, Sussex, UK.

<sup>h</sup>Department of Earth Sciences, University of Minnesota, Minneapolis, MN 55455, USA.

<sup>i</sup>Key Laboratory of Karst Dynamics, Ministry of Land and Resources, Institute of Karst Geology, Chinese Academy of Geological Sciences, 541004 Guilin, China.

<sup>1</sup> To whom correspondence may be addressed: Email (GK) [kathayat@xjtu.edu.cn](mailto:kathayat@xjtu.edu.cn); (AS) [asinha@csudh.edu](mailto:asinha@csudh.edu); (HC) [cheng021@xjtu.edu.cn](mailto:cheng021@xjtu.edu.cn)

Author contributions: G.K. & A.S. designed the research; G.K., A.S., S.F.M.B., L.T., C.S., H.L., X.D., H.Z., Y.N., R.A., V.D., R.L.E., and H.C. performed the research; G.K. and A.S. analyzed the data and wrote the paper.

**Competing interests:** The authors declare no competing interests.

**Classification:** Physical Sciences/Earth, Atmospheric, and Planetary Sciences

**Keywords:** Indian Summer Monsoon; Droughts; Societal Changes; De-Industrialization

### This PDF file includes:

Main Text  
Figures 1 to 4

49 **Abstract**

50 Protracted droughts, lasting years to decades, constitute severe threats to human welfare across the  
51 Indian subcontinent. Such events are, however, rare during the instrumental period (c. since 1871  
52 CE). In contrast, the historic documentary evidence indicates the repeated occurrences of protracted  
53 droughts in the region during the pre-instrumental period implying that either the instrumental period  
54 underestimates the full spectrum of monsoon variability, or the historic accounts overestimate the  
55 severity and duration of the past droughts. Here we present a temporally precise speleothem-based  
56 oxygen isotope reconstruction of the Indian summer monsoon precipitation variability from  
57 Mawmluh cave located in Northeast India. Our data reveal that protracted droughts, embedded within  
58 multidecadal intervals of reduced monsoon rainfall, frequently occurred over the past millennium.  
59 These extreme events are in striking synchrony with the historically documented droughts, famines,  
60 and geopolitical changes in India. Our findings necessitate reconsideration of the region’s current  
61 water resources, sustainability, and mitigation policies that discount the possibility of protracted  
62 droughts in the future.

63

64 **Significance**

65 Severe and long-lasting droughts represent one of the greatest potential threats to human welfare in  
66 the Indian subcontinent. While historical documentary sources from the region provide vivid accounts  
67 of catastrophic drought-related famines and mass mortalities events, these accounts are fragmentary,  
68 and their veracity cannot be always confirmed. In this study, we have used stalagmites from Northeast  
69 India to reconstruct a history of Indian summer monsoon droughts over most portions of the last  
70 millennium with an unprecedented dating accuracy. Our reconstructed drought history is in striking  
71 synchrony with the historical evidence, where available, and provides important context against which  
72 the key geopolitical and societal changes and their links to climate can be assessed.

73

74 **Introduction**

75 Spatially widespread multi-year failures of the Indian summer monsoon (ISM) potentially pose one of  
76 the most serious threats to human welfare and India’s vast monsoon-centric agriculture sector, which  
77 contributes ~20% to its gross domestic product and employs nearly 60% of the workforce (1).  
78 However, such events have rarely occurred during the instrumental period (~ the last 150 years).  
79 Various time series of the area-weighted rainfall such as the ‘All India Summer Monsoon Rainfall’  
80 (hereafter, AIR) (2), depict a monsoon system that appears to be remarkably stable over the  
81 instrumental period with rainfall oscillating biennially within a narrow range ( $\pm 10\%$  or  $\sim \pm 1$  standard  
82 deviation of the long-term mean  $\sim 900$  mm) (3). There are sporadic aberrations in ISM rainfall  
83 manifesting as a 10-15 % reduction in the AIR—a widely used metric for defining droughts (or  
84 “deficient rainfall”) over India (4). By this metric, India has experienced 27 droughts during the  
85 instrumental period with only one instance of a three-year consecutive drought (1985-1987 CE) (*SI*  
86 *Appendix, Fig. S1a*). Subcontinent-wide severe droughts or “monsoon failures” ( $>2$  standard  
87 deviations departures in AIR) are rare with only five such instances over the last 150 years, including  
88 the one in 1877 CE when the AIR fell  $\sim 30\%$  below the mean (*SI Appendix, Fig. S1a*) with devastating  
89 societal consequences (5). Instrumental observations also provide a hint to the quasi-oscillatory  
90 variability in ISM rainfall that appears to promote higher frequencies of droughts and pluvials over  
91 multidecadal periods of weaker and stronger monsoon, respectively (6). For example,  $\sim 10$  droughts  
92 occurred between the 1960s and 1990s whereas only 4 droughts took place between the 1930s and  
93 1960s (*SI Appendix, Fig. S1b*).

94

95 In contrast to the instrumental period, the historical documentary evidence and high-resolution proxy  
96 records paint a drastically different picture of ISM drought characteristics during the past millennium  
97 and beyond. For example, classical ancient Indian texts such as *Arthshastra* (c. 150 CE) and *Rigveda*  
98 (c. 1500 BCE) contain numerous accounts of continuous multi-year droughts and ensuing famines,  
99 with some lasting for as long as 12 years (7). Periods of protracted droughts (defined here as droughts  
100 lasting for >3 consecutive years and/or multidecadal periods with drought every other or every third  
101 year) are evident in the systematic compilations of historical droughts and famines that occurred  
102 between ~ 1500 CE and 1900 CE (8-12) (*SI Appendix, Text S1*). Reconstructions of ISM variability  
103 based on high-resolution proxy archives such as Himalayan ice cores (13), speleothems from central  
104 (14-17) and northern (18-19) India, the Arabian Peninsula (20), Southeast Asia (21), and the gridded-  
105 tree-ring network over Asia (22-24) also indicate extended periods of droughts that broadly agree with  
106 the historic evidence of droughts and famines over the last 500 years.

107  
108 Empirical and modeling considerations have alternately conceptualized ISM as a self-regulating  
109 coupled ocean-atmosphere system that tends to remain within a narrow range (3) or a system prone to  
110 abrupt non-linear transitions between strong and weak states in response to changes in internal  
111 feedback mechanisms (16, 25). Understanding which of the two mechanisms, if either, will dictate the  
112 future behavior of ISM in a warming climate holds enormous societal implications. An extended  
113 record of ISM natural drought variability is, therefore, a vital estimate for assessing the true range of  
114 past climate variability and the degree to which is represented in climate models. In this study, we  
115 have constructed a sub-annually resolved and precisely dated (average  $1\sigma$  error  $\pm$  4 years) speleothem  
116 record from Mawmluh cave, located near the town of Cherrapunji (25°15'32"N, 91°42'45"E, 1290 m  
117 above sea level) at the southern fringe of Meghalaya Plateau in Northeast India (NEI) (*SI Appendix,*  
118 *Fig. S2*). Our data together with the historical evidence of droughts provide key insights into the ISM  
119 drought history over the past millennium (~1080 to 1905 CE). Our new reconstruction represents a  
120 marked improvement over previous speleothem-based reconstructions from the region and provides  
121 critical targets for climate models and a robust hydroclimatic context against which the key  
122 geopolitical and societal changes and their links to climate can be assessed.

## 123 124 **Results and Discussion**

125 **Speleothem Paleoclimate Record.** The paleoclimate record for this study is established by ~1545  
126 paired measurements of stable oxygen ( $\delta^{18}\text{O}$ ) and carbon ( $\delta^{13}\text{C}$ ) isotope from two stalagmites (ML-5  
127 and ML-8) from Mawmluh cave (25°15'32"N, 91°42'45"E, 1290 m above the sea level) (*SI Appendix,*  
128 *Table S1*). The chronology is tightly constrained by 14 and 4  $^{230}\text{Th}$  dates, respectively. The ML-5 and  
129 ML-8 samples have very high uranium concentrations (> 600 parts per billion (ppb)) and low detrital  
130  $^{232}\text{Th}$  concentrations (~ 62 to 250 parts per trillion (ppt)) that allow us to obtain accurate ages with an  
131 average age uncertainty of ~ 4 years ( $1\sigma$ ) years (*SI Appendix, Table S2*). The age model for each of  
132 the  $\delta^{18}\text{O}$  profiles was constructed by generating 2000 age realizations using the COPRA (Construction  
133 of Proxy Record from Age models) age-modeling routine (26), and the median ages are used as final  
134 age models (*SI Appendix, Fig. S3*) (*Materials and Methods*). Statistically significant replication  
135 between the ML-5 and ML-8  $\delta^{18}\text{O}$  profiles during their contemporaneous growth period (~1739 and  
136 1854 CE,  $N=116$ ,  $r=0.33$ ,  $p=0.02$ , after accounting for serial autocorrelation in each time series)  
137 on their independent age models suggests that the records contain a common climate signal (*SI*  
138 *Appendix, Text S2, and Fig. S4*). The ML-5 and ML-8  $\delta^{18}\text{O}$  profiles were stacked together (hereafter,  
139 MAW) in such that the “composite” record consists of the ML-5 isotopic values until c. 1854, and the  
140 ML-8 isotopic values afterward to 1906 CE. After stacking, the record was de-noised and detrended

141 (*SI Appendix, Fig. S5*, also see *Materials and Methods*) to yield a continuous record that spans from ~  
142 1080 to 1906 CE with an average temporal resolution and age uncertainty of ~ 0.6 and ~ 4 years ( $1\sigma$ )  
143 years, respectively (Fig. 1).

144 **Proxy Interpretation.** Mawmluh cave is located in one of the wettest places on Earth with an  
145 average annual precipitation of over ~11,000 mm, with 70-80% of precipitation falling during the  
146 JJAS (June-August) (*SI Appendix, Fig. S2*) (27). On intra-seasonal to interannual timescales, rainfall  
147 over NEI and the rest of the Indian sub-continent exhibits a quasi-east-west precipitation dipole with  
148 anomalies of one sign over NEI and of an inverse sign over North, Northwest, and Central India (16,  
149 27) (Fig. 2, a and f). Previously, we used an isotope-incorporated Global Spectral Model version 2  
150 (IsoGSM2) with moisture-tagging capability (28) to show that changes in the relative moisture  
151 contributions from different moisture source regions drive much of the observed interannual  
152 variability in the oxygen isotope composition of precipitation ( $\delta^{18}\text{O}_p$ ) and its amount over the Indian  
153 subcontinent (29). Our previous work indicates that during weak monsoon years, the zonal moisture  
154 flux is anomalously enhanced across North India (with its core at ~25°N) via a northward shifted low  
155 level-jet (LLJ) over the Arabian Sea and across continental India, which serves as a conduit for  
156 transporting moisture from the Arabian Sea/Red Sea moisture source region (hereafter, ARAB) over a  
157 large northwest-southeast trending region that extends from the Arabian Peninsula to Southeast Asia  
158 (Fig. 2, b and c). This zonal moisture flux exports  $^{18}\text{O}$ -enriched moisture from the Arabian Sea along  
159 the Indo-Gangetic plains to NEI, where Mawmluh cave is located. Consequently, during weak  
160 monsoon years, the relative contribution of moisture originating from the ARAB dominates over  
161 much of the Indian subcontinent, including over NEI, while moisture from the remote portion of the  
162 Indian Ocean has a greater influence during strong ISM years (29-30). Indeed, time series  
163 comparisons between the simulated  $\delta^{18}\text{O}_p$  and ARAB (i.e., % fraction of total precipitable water  
164 (TPW)) extracted from the grid cell nearest to Mawmluh cave show statistically significant negative  
165 and positive correlations with precipitation amount, respectively over much of the subcontinental  
166 India, approximately west of 85° E longitude (Fig. 2, b-f and *SI Appendix, Fig. S6*). These dynamical  
167 constraints, therefore, explain the intriguing situation that the  $\delta^{18}\text{O}_p$  of summer monsoon rainfall at  
168 NEI, despite being located at the opposite end of the precipitation dipole, reflects upstream changes in  
169 monsoon precipitation amount over North, Northwest, and Central India (~ 15-28°N and 70-84°E)  
170 (via the moisture source effect rather than the ‘classical’ amount effect). This line of reasoning is  
171 strongly supported by the strong positive correlation between the MAW  $\delta^{18}\text{O}$  record and the first  
172 principal component (PC1) of ~ 15 tree ring width chronologies (31) from NEI in such that positive  
173 speleothem  $\delta^{18}\text{O}$  values (i.e., reflecting drier conditions in Northwest/North/Central India) covary  
174 with the higher values of PC1 (i.e., wetter NEI) and vice-versa between 1700 and 1900 CE (*SI*  
175 *Appendix, Fig. S7*). Following this reasoning (fully described in ref. 29), we interpret temporal  
176 variations in the MAW  $\delta^{18}\text{O}$  record to be a sensitive indicator of precipitation variability over a broad  
177 region roughly west of 85°E longitude over subcontinental India.

178

179 The detrended z-score transformed MAW  $\delta^{18}\text{O}$  profile exhibits prominent inter-annual and quasi-  
180 oscillatory multidecadal-centennial scale variability (Fig. 1c, *SI Appendix, Fig. S8*). The multidecadal  
181 episodes of inferred weaker and stronger ISM rainfall are highlighted by a 30-year lowpass filter.  
182 Embedded within the weaker episodes of ISM are sustained intervals with high z-score values (>1),  
183 which we interpret as drought-like conditions. An important caveat regarding this interpretation is that  
184 the memory effects in the overlying karst might lead to an overestimate of the duration of these  
185 episodes but an underestimate of their amplitude. Comparisons of the MAW  $\delta^{18}\text{O}$  profile with the  
186 existing high-resolution speleothem records of ISM from the North, Central, and Northeast India (14-

187 19), the Arabian Peninsula (20), and Southeast Asia (21) indicate broad similarities but also some  
188 differences (*SI Appendix, Fig. S9*). The latter is to be expected owing to the dating errors and the  
189 unique karst characteristics of each cave site that lead to the homogenization of meteoric waters to a  
190 varying degree. Notwithstanding, the general pattern of multidecadal to centennial timescale  
191 variability is similar across all records during the past millennium. More importantly, however, the  
192 inferred intervals of extreme droughts identified in the MAW record are also evident in other regional  
193 speleothem records (based on > 90 percentile values of normalized and detrended time series of each  
194 record) (Fig. 3 and *SI Appendix, Fig. S9*). We note that some existing records from NEI do not have  
195 sufficiently high dating precision, temporal resolution, and robust chronological framework (16, 32-  
196 34) and therefore, these records were excluded from this comparison.

197  
198 **Hydroclimatic Extremes and Societal Changes.** The precise chronology of the MAW record allows  
199 a direct comparison with historically documented droughts and famines for the period between 1500  
200 and 1900 CE (*SI Appendix, Text S1*). Although the ‘drought’ compilations (8-11) were constructed by  
201 painstakingly extracting information from a variety of documentary sources (*SI Appendix, Text S1*),  
202 one important caveat exists that the drought chronology for the 1500s-1770s is essentially that of  
203 famines (10). While famines typically result from a combination of societal, political, and  
204 environmental reasons, the vast majority of famines in India before the British period were ultimately  
205 caused by drought-induced harvest failures (35). It is, therefore, not unreasonable to assume that the  
206 droughts were the dominant reason for famines during the period between the 1500s and 1770s.

207  
208 A comparison of the historic drought chronology with the MAW profile is highlighted by using a  
209 centered 30-year sliding mean of the drought recurrences as reported in ref (11) (Fig. 3). Notably,  
210 three multidecadal periods of high drought frequencies (~ 8-14 droughts per 30 years) in the historical  
211 data (the 1560s-1640, 1780s-1810s, and 1850s -1870s) are in excellent temporal agreements with the  
212 inferred periods of weaker ISM inferred from our data (Fig. 3). For most portions between the 1500s  
213 and 1900s, the historic drought frequencies are similar to the instrumental period (averaging about 4-8  
214 droughts per 30 years). **The periods of low drought frequencies indicated from historical evidence  
215 conform generally well with the pluvial conditions inferred from our MAW record. Notably, three  
216 multidecadal periods of higher drought frequencies (~ 8-14 droughts per 30 years) in the historical  
217 data (the 1550s-1640, 1780s-1810s, and 1850s-1870s) are in excellent temporal agreements with the  
218 inferred periods of weaker ISM inferred from our data (Fig. 3). There are, however, also few  
219 instances of apparent mismatch between the proxy and historical data. For example, the weak  
220 monsoon period from the 1550s to 1640s deduced from the historical drought compilations appears to  
221 be inflated compared to the proxy data (Fig.3).**

222  
223 The 1780s to 1810s stand out as an exceptional interval in both historical and proxy data. The historic  
224 drought compilations for this period principally draw their information almost exclusively from one  
225 East India Company report by F.C. Danvers, a British officer with the company. His report, in turn,  
226 was compiled from contemporary accounts of droughts and famines from various regions of the  
227 subcontinent. Danvers’ report—*A Century of Famines* (36), shows that there were at least 11 drought-  
228 related famines during this period, six of which, including the well-known Chalisa and Doji Bara or  
229 Skull Famines, occurred between ~1782 and 1792 CE (Fig. 4), with a combined estimated death toll  
230 in the excess of 11 million, making it one of the deadliest decades in Indian history (8-11, 37). The z-  
231 score values in the MAW record between 1780 and 1810 CE are among the highest and occurred in  
232 striking temporal agreement with large positive  $\delta^{18}\text{O}$  excursions in other regional speleothem records  
233 and the largest chloride/dust spikes in the Himalayan ice core record (Fig. 3 and *SI Appendix, Fig. S9*)

234 which are interpreted to reflect greater aridity and enhanced dust transport from the Indian peninsula  
235 (13) indicating severe drought conditions.

236

237 Mutually corroborating proxy and historical evidence for severe droughts in the late 18<sup>th</sup> and early  
238 19<sup>th</sup> centuries shed new light on the possible role of climate as a contributing factor that led to India's  
239 deindustrialization between ~ the 1750s and 1860s (38) (Fig. 4 and *SI Appendix, Fig. S10*). At the  
240 peak of the Mughal Empire (c. 1650-1700 CE) India was manufacturing and exporting ~25% of the  
241 world's textiles. However, by the middle of the 19th century, India had lost most of its export market,  
242 predominantly to the British Empire (*SI Appendix, Text S1*). While the exact mechanisms of  
243 deindustrialization were complex and global in scope, it has been argued that the fragmentation of the  
244 Mughal Empire and reduced agricultural productivity, severely limited the supply of grains, resulting  
245 in sharp rises in the prices and nominal wages in the cotton and weaving industry, precipitated the  
246 first phase (~ CE 1780s to 1810s) of deindustrialization (38). Our data place the early phase of  
247 deindustrialization into the most severe 30-year spell of weaker ISM of the entire past millennium  
248 thus, supporting the hypothesis that a drastic slump in agricultural productivity together with the  
249 fragmentation of the Mughal Empire sowed the seeds of India's deindustrialization (Fig. 4 and *SI*  
250 *Appendix, Text S1 and Fig. S10*).

251

252 The 1550s to 1640s stand out as another interval of coherence between the historical and proxy data.  
253 Within this near-century-long interval of weaker ISM, the MAW record indicates ~25 years of  
254 sustained high z-score values (>1) between ~1595 and 1620 CE that are co-eval with the prominent  
255 dust spikes in the Himalayan ice core record (13) and extreme positive  $\delta^{18}\text{O}$  excursions in the regional  
256 speleothem records (14-21) indicating severe drought conditions (Fig. 3). The drought compilations  
257 for this period extract information from textual documents composed in Farsi during the reigns of the  
258 prominent Mughal emperors such as Akbar (1556–1605 CE), Jehangir (1605–1628 CE), Shah Jahan  
259 (1628–1659 CE), and Aurangzeb (1659–1707 CE) (39). These court chronicles, for example, the  
260 *Akbarnama* (the book of Akbar) and *Ain-I Akbari* (the regulations of Akbar) provide vivid accounts of  
261 droughts and famines during this period, including the “Deccan Famine” (1630–1632 CE) — one of  
262 the most devastating mass mortality events in recorded Indian history (Fig. 4 and *SI Appendix, Text*  
263 *S1*). This period also coincides (within age uncertainties) with the collapse of the Guge Kingdom in  
264 western Tibet (19) and with the abandonment of Fatehpur Sikri (40), one of the largest cities of its  
265 time that briefly served as the capital of the Mughal Empire (c. 1571 to 1585 CE) under the reign of  
266 Akbar, before it was completely abandoned by 1610 CE (Fig. 4 and *SI Appendix, Text, S1 and Fig.*  
267 *S10*). Intense debates surround the circumstances under which the city was abandoned, with most  
268 historians attributing it to a range of political and military reasons, although extreme droughts and the  
269 ensuing loss of water supply have also been proposed (40-41). Our data support the latter suggestion  
270 as it places the abandonment phase of Fatehpur Sikri well within one of the driest multidecadal  
271 episodes (~1580-1610 CE) of the past millennium (Figs. 4 and *SI Appendix, Fig. S10*).

272

273 Striking accordance between our data and the historic drought chronology indicates that the MAW  
274 record can be reliably used to extend back the ISM drought variability for periods where the historic  
275 information is fragmentary or unreliable. Our data reveal a prominent near century-long interval of  
276 weaker ISM between the second half of the 13<sup>th</sup> and early 14<sup>th</sup> centuries, with peak drier conditions  
277 between ~ 1290 and 1310 CE (Fig. 3). The scattered documentary evidence from this period indicates  
278 frequent multi-year droughts in northern India between ~1296-1316 CE (e.g., refs. 11 and 42) under  
279 the reign of *Alauddin Khilji*, one of the several dynastic rulers of the ‘Delhi Sultanate’ that preceded  
280 the Mughal Empire (Fig. 4). Additionally, fragmentary historic and archaeological evidence from

281 western Tibet indicates important political, environmental, and social changes in the region. Between  
282 ~950 and 1350 CE, western Tibet was under a confederacy rule by Purang, Guge, and Maryul polities  
283 (43). Historical sources speak of a gradual decline in the polity after ~ 1200 CE with a complete  
284 collapse by ~ 1350 CE (44). Although the historical documents describe this collapse primarily in  
285 political terms, archaeological evidence from the Sutlej Valley indicates settlement abandonment, a  
286 significant drop in the water table, and stranded major irrigation systems that are tentatively dated to  
287 the period CE 1250 and 1300 (15), coinciding within the period of severe weakening in the ISM (Fig.  
288 4).

289  
290 **Extreme Droughts and Pluvials.** One notable feature of the MAW record is the presence of abrupt  
291 and extremely positive  $\delta^{18}\text{O}$  excursions (exceeding 2 or even 3 standard deviations) against the mean  
292 state of both weaker and stronger monsoon conditions (Fig. 4). We interpret these as episodes of  
293 ‘extreme’ droughts. One such event in our record centered at ~ 1400 CE occurred tantalizingly close  
294 to the “Durga Devi Famine”—one of the most widely referenced famines (1395 to 1408 CE) in the  
295 historic accounts (7-11) that struck large parts of western India (Fig. 4, *SI Appendix, Text S1*). Another  
296 event centered at ~ 1640 CE constituting the largest positive  $\delta^{18}\text{O}$  excursion in our record, coincided  
297 with the so-called “Ming Dynasty drought” (~1638-1641 CE) that affected large parts of northern  
298 China and India (22, 45). The closest modern analog of these extreme events is the drought of 1877  
299 when the AIR fell more than 3 standard deviations against the backdrop of a stronger monsoon (*SI*  
300 *Appendix, Fig. S1*). The 1877 drought was a regional expression of a globally orchestrated period of  
301 climate anomalies that coincided with a strong El Niño, which immediately followed the preceding  
302 six years of strong La Niña conditions (5). We note here that the 1877 drought is, however, weakly  
303 expressed in our record likely because a single season of  $^{18}\text{O}$ -enriched low rainfall amount may not be  
304 sufficient to skew the  $\delta^{18}\text{O}$  of speleothem to more positive values due to the mixing of meteoric  
305 waters in the overlying karst. In addition to extreme droughts, our record also contains evidence for  
306 the presence of extreme pluvial conditions. **For example, the first half of the 19<sup>th</sup> century in our record**  
307 **is marked by an exceptional wet phase of ~35 years (CE 1810–1845), which came on the heels of one**  
308 **of the driest ISM episodes (~ CE 1780s-1810s) in our record (Figs. 3, 4). We estimate that this**  
309 **extreme dry to extreme wet transition occurred well within less than a decade and may represent an**  
310 **extreme manifestation of ISM, which is prone to abrupt non-linear transitions in response to changes**  
311 **in internal feedback mechanisms (16, 25).**

312  
313 **ENSO and ISM Droughts.** Historic documentary and proxy evidence discussed above make an  
314 intriguing case that ISM can periodically “lock” into a drought-prone mode that may last for decades  
315 (15-16). Understanding what climate dynamics triggered and sustained such extended periods of  
316 drought during the past millennium is vital to estimating the likelihood of their reoccurrence in the  
317 future. ISM droughts have been generally attributed to changes in the El Niño Southern Oscillation  
318 (ENSO) (46), sea surface temperature (SST) anomalies in the Indian (47), and Atlantic (48) Oceans,  
319 and internal dynamics (49). While detailed examinations of the potential causative mechanisms  
320 require coordinated proxy-modeling efforts that are outside the scope of this paper, here below we  
321 briefly explore the role of El Niño in causing the ISM droughts during the past millennium by cross-  
322 examining the historical and proxy-based reconstructions of ENSO with our record.

323  
324 Time series analysis of the MAW record in both frequency and temporal domains reveals intermittent  
325 but prominent periodicities in the interannual band of ENSO (~2-8 years) (*SI Appendix, Fig. S8*)  
326 consistent with similar spectral estimates detected in existing speleothem records from the region (17-

327 18) including a temporally short (~1960s to 2010s) but ultra-high resolution (~0.1 year) speleothem  
328 record from Mawmluh cave (34). Intermittent presence of the ENSO band, particularly before the  
329 ~1250s and after ~1650s, is quite like the waxing and waning of the ENSO-ISM relationship observed  
330 during the instrumental period (50), and thus, in the long-term context of our data, the supposed  
331 “breakdown” of this relationship since the 1980s (51) is not that unusual. Furthermore, comparisons  
332 of the MAW record to a large array of tree-ring and coral-based reconstructions of ENSO (*SI*  
333 *Appendix, Fig. S11*) reveal no clear or consistent relationship between the multidecadal periods of  
334 enhanced ENSO variance and ISM droughts, due in part, to large divergence among the various  
335 ENSO reconstructions during the pre-industrial period.

336

337 We also compared the historic droughts chronology (11) to two historic El Niño events chronologies  
338 constructed from textual documentary evidence from northern Peru (52), a region of heightened  
339 sensitivity to ENSO, and global multiproxy data blended with historical documentary sources for the  
340 period between 1525 and 1900 CE (53). Both chronologies show broad qualitative similarities in the  
341 evolution of El Niño activity but differ markedly in terms of the number of identified El Niño events  
342 (*SI Appendix, Fig. S12*). The chronology in ref. 52 likely underestimates El Niño events, as not all  
343 events result in precipitation extremes in northern Peru, whereas the latter chronology (53) is likely an  
344 overestimation because it includes several instances of historic ISM droughts as a proxy of El Niño,  
345 which is problematic because not all El Niño events produce droughts over India (54).  
346 Notwithstanding these caveats, both chronologies show notable multidecadal scale peaks in El Niño  
347 activity centered in the 1640s, 1720s, 1800s, and ~1880s. While the peaks in El Niño activity in the  
348 1640s and 1800s correspond with the increased historical drought frequency (*SI Appendix, Fig. S12*).  
349 On an event-by-event basis comparison, only ~20% and ~50 % of the historic droughts may have co-  
350 occurred with El Niño events as reported in refs. 52 and 53, respectively—an association not unlike  
351 during the instrumental period, where ~ 50% of the ISM droughts have co-occurred with the El Niño  
352 events (54) (*SI Appendix, Fig. S1*).

353

354 In summary, historical documentary and proxy evidence presented in this paper show that the ISM  
355 drought history during the past millennium was characterized by decadal to multidecadal periods of  
356 protracted droughts. This view of the ISM system stands in stark contrast with the instrumental  
357 period, whose apparent stability might lead one to incorrectly surmise that neither **protracted droughts**  
358 **nor frequently occurring droughts are intrinsic aspects of its variability**. This seemingly reassuring but  
359 rather myopic view currently informs the region’s present-day water resource infrastructure and  
360 contingencies policies and discounts the possibility of protracted monsoon failures in the future (15-  
361 17). Recurrence of protracted monsoon failures as documented here can easily overwhelm the  
362 adaptive capabilities of modern societies unless a longer-term and holistic understanding of monsoon  
363 variability is incorporated into drought management and mitigation planning.

364

## 365 **Materials and Methods**

366 **Field Collection and Sample Preparation.** Mawmluh cave (25°15' N, 91°42' E, 1290 m above sea level)  
367 is located near the town of Sohra (Cherrapunji) at the southern fringe of the Meghalaya Plateau, Northeast  
368 India. The cave is overlain by a total overburden of ~30-100 m, consisting of limestone, sandstone, a 0.5-1  
369 m thick layer of coal, and a thin soil cover (<15 cm), which permits the short residence time of seasonal  
370 changes in precipitation (59). In most portions of the cave, relative humidity is >95%. The vegetation  
371 above the cave is sparse, mostly consisting of grasses, shrubs, and bushes. Only dolines hold remnants of  
372 forest, which today are held sacred. Two stalagmites – ML-5 (~128.5 mm) and ML-8 (~55.40 mm) – were  
373 collected ~300-500 m from the cave’s entrance in February 2015. The cave’s ambient temperature and  
374 relative humidity (RH) at the time of sample collection were ~18.0 °C and 98%, respectively. A multi-

375 annual monitoring program, conducted between 2007 and 2014, characterizes the cave's hydrochemistry  
376 and ventilation dynamics (59). The stalagmites were cut with a thin diamond blade along the growth axes  
377 and polished. Subsamples for  $^{230}\text{Th}$  dating (weighing typically between 200 and 300  $\mu\text{g}$ ) were obtained by  
378 drilling with a 0.5 mm carbide dental burr. An automated triaxial micro mill (New Wave Micromill) was  
379 used to obtain subsamples for stable isotopic analyses by continuously milling at 50  $\mu\text{m}$  increments along  
380 the growth axis of ML-5 (between ~18 and 128.5 mm with 0 being the top where the isotopic sampling  
381 was initiated) and at 100  $\mu\text{m}$  for ML-8 (between 0 and 55.40 mm, with 0 being the top where the isotopic  
382 sampling was initiated) (*SI Appendix, Table S1*). Both ML-5 and ML-8 samples are characterized by the  
383 presence of thin (~ 15-20 mm) whitish aragonitic layers (*SI Appendix, Fig. S3*). We discarded samples  
384 from this layer because the previous cave studies from the Mawmluh cave have shown that this  
385 distinctive layer was pervasively deposited over a large number of stalagmites, flowstones, and  
386 stalactites in the cave since the post-1950s' marking the onset of large-scale limestone mining  
387 operation above the Mawmluh cave, which resulted in extensive fracturing of bedrock and the rapid  
388 infiltration of meteoric waters into the cave. The oxygen and carbon isotopic values from this  
389 aragonite layer are in isotopic disequilibrium and not representative of the values expected from  
390 natural climate variability (59).

391  
392 **Stable Isotope Measurements.** The ML-5 and ML-8 isotope profiles consist of 1286 and 259 stable  
393 isotope measurements, respectively (Fig. 1, *SI Appendix, Table S1, and Fig. S13*). Subsamples for  $\delta^{18}\text{O}$   
394 and  $\delta^{13}\text{C}$  analyses were measured using a Finnigan MAT 253 mass spectrometer coupled with an online  
395 carbonate preparation system (Kiel IV) at the Isotope Laboratory, Xi'an Jiaotong University, Xi'an, China.  
396 All results are reported per mil (‰) relative to the Vienna Pee Dee Belemnite (VPDB) standard. The long-  
397 term precision of the Vienna Pee Dee Belemnite standard for the  $\delta^{18}\text{O}$  and  $\delta^{13}\text{C}$  was ~0.08 ‰. Duplicate  
398 measurements of standards NBS19 and TTB1 show a long-term reproducibility of ~0.1‰ (1 $\sigma$ ) or better.  
399

400  **$^{230}\text{Th}$  Dating.** The chronological frameworks of ML-5 and ML-8 records were established by 14, and 4  
401  $^{230}\text{Th}$  dates, respectively (*SI Appendix, Table S2*).  $^{230}\text{Th}$  dating was performed at Xi'an Jiaotong  
402 University, China, by using Thermo Finnigan Neptune plus multi-collector inductively coupled plasma  
403 mass spectrometers. We used standard chemistry procedures (60) to separate uranium and thorium. A  
404 triple-spike ( $^{229}\text{Th}$ - $^{233}\text{U}$ - $^{236}\text{U}$ ) isotope dilution method was used to correct instrumental fractionation and to  
405 determine U/Th isotopic ratios and concentrations (61). U and Th isotopes were measured on a MasCom  
406 multiplier behind the retarding potential quadrupole in the peak-jumping mode using standard procedures  
407 (61). Uncertainties in U/Th isotopic measurements were calculated offline at the 2 $\sigma$  level, including  
408 corrections for blanks, multiplier dark noise, abundance sensitivity, and contents of the same nuclides in  
409 spike solution. Corrected  $^{230}\text{Th}$  ages assume an initial  $^{230}\text{Th}/^{232}\text{Th}$  atomic ratio of  $4.4 \pm 2.2 \times 10^{-6}$ , and a  
410 bulk earth  $^{232}\text{Th}/^{238}\text{U}$  value of 3.8 for material at secular equilibrium (61). We have reported the age  
411 uncertainties at 1 $\sigma$  level by arbitrary assuming a 25% error.  
412

413 **Age Models and Composite Record.** The ML-5 and ML-8 age models and associated age uncertainties  
414 were modeled using the COPRA routine (26). We used 2,000 Monte Carlo age model realizations to  
415 account for the dating uncertainties and the median and the 2.5 and 97.5% quantile confidence limits were  
416 used in the final age model. ML-5 and ML-8 have a sub-annual temporal resolution, respectively. The ML-  
417 5 and ML-8 isotope profiles span from 1080 to 1854 CE and 1738 to 1906, respectively. The ML-8 isotope  
418 profiles were stacked with ML-5 at 1854.65 CE to derive the final composite MAW record with a sub-  
419 annual average resolution (*SI Appendix, Fig. S3*). Statistically significant replication between the ML-5  
420 and ML-8  $\delta^{18}\text{O}$  profiles during their contemporaneous growth period (~1739 and 1854 CE,  $N=116$ ,  $r$   
421  $= 0.33$ ,  $p = 0.02$ ), on their independent age models allow us to generate a composite record by  
422 stacking the ML-5 and ML-8  $\delta^{18}\text{O}$  profiles at ~1854 CE. For the contemporaneous interval from 1739  
423 to 1854 CE, the ML-5 sample was selected as the main record because of its higher age precision in  
424 comparison with ML-8. The portion from 1854 to 1906 CE is derived from ML-8 (*SI Appendix, Fig.*  
425 *S4*).

#### 427 **Statistical Analyses**

428 **Removing the Noise from the Composite Record.** The composite MAW  $\delta^{18}\text{O}$  record exhibits prominent  
429 high-frequency oscillations (Fig. 1 and *SI Appendix, Fig. S4*) due to extremely high temporal resolution

430 (mean ~0.6 years) and the low water residence time in Mawmluh cave (59). This high-frequency signal  
431 likely reflects the mixed  $\delta^{18}\text{O}$  of meteoric waters from (mostly ISM) rainfall throughout the year. We  
432 removed this high frequency ‘noise’ using the ensemble empirical mode decomposition (EEMD) algorithm  
433 (55), which is an adaptive data decomposition method for analyzing nonstationary and nonlinear time  
434 series. EEMD uses an ensemble distribution of data generated by adding white noise to the source data and  
435 then iteratively removes the highest frequency oscillatory components superimposed on lower frequency  
436 signals. We de-noised the  $\delta^{18}\text{O}$  data by removing the first component of the EEMD decomposition (Fig. 1  
437 and *SI Appendix, Fig. S5*). The lag-1 autocorrelation of the first EEMD component is -0.39, lag-2 is 0.12,  
438 and lag-3 is even smaller (0.03), indicative of characteristic white noise.

439  
440 **Trend Removal of the De-noised Record.** To highlight the sub-decadal to multi-decadal variability, we  
441 used singular spectrum analysis (SSA) to remove the nonlinear trends (>200 years) from the de-noised  
442 records (Fig. 1 and *SI Appendix, Fig. S5*). The SSA method decomposes time series into monotonic and  
443 oscillatory modes of variability (56). We detrended the composite record by removing the first component  
444 (i.e., the largest eigenvalue from an autocovariance matrix of SSA). The size of the embedded window was  
445 set to one-fifth the size of the length of the time series. The denoised and detrended time series was  
446 normalized by its mean and standard deviation to produce z scores and was interpolated to 0.6 and 1-year  
447 resolution (Fig. 1 and *SI Appendix, Fig. S5*) for better comparison with other time series. The 0.6-year  
448 interpolated version was used for the spectral and wavelet analysis.

449  
450 **Spectral and Wavelet Analysis.** Periodic variations in the de-noised and detrended time series were  
451 assessed by the multi-taper method (MTM) using a half-bandwidth parameter of 2 that represents the  
452 optimal compromise between spectral resolution and variance (62). Because interpolation procedures  
453 might introduce artifacts, potentially biasing derived frequencies, we also conducted a parallel analysis on  
454 un-interpolated denoised and detrended data using the Lomb–Scargle approach (63). The latter utilizes the  
455 unevenly spaced data and provides an independent check for any such artifacts. All power spectra were  
456 assessed only up to a conservative assessment of the Nyquist frequency (i.e., up to a frequency  
457 approximately twice the average sample frequency). We quantified the effect of age model errors by  
458 conducting MTM (62) and Lomb–Scargle (63) procedures on the 2,000 age model realizations from  
459 COPRA to obtain uncertainty bands for the estimated spectrum. Peaks were tested for significance relative  
460 to the null hypothesis of a globally red noise background, estimated empirically from the first-order  
461 autoregressive [AR(1)] character of the data. We tested the significance of spectral peaks by comparing  
462 them against simulated 2000 AR-1 nulls and estimating the 5-95% quantile of this distribution. Only  
463 spectra outside the AR1 envelope are deemed significant. Wavelet analysis was performed using  
464 procedures described in (64).

465  
466 **Strong and Weak Years Composites.** The strong (1983, 1988, and 1994) and weak (1982, 1987, 2002,  
467 2004, and 2009) ISM seasons as shown in figure 2 panels are defined as positive (negative) departures of  
468 one standard deviation from the mean of All India Rainfall (4).

469  
470 **Field and Linear Correlations and Significance.** The statistical significance of field correlations is  
471 calculated using the false discovery rate (FDR) procedure (58) to control the proportion ( $q = 5\%$ ) of  
472 erroneously rejected null hypotheses using a MATLAB code (65), where  $q$  guarantees that 5% or fewer of  
473 the locations where the null hypothesis is rejected are false detections. The statistical significance of linear  
474 trends and correlation coefficients (95% confidence intervals and P values) reported in this paper, where  
475 appropriate, account for the autocorrelation of time series.

476  
477 **IsoGSM2.** We used an isotope-enabled general circulation climate model version 2 (IsoGSM2) (66)  
478 together with the moisture-tagging (29) simulation data to understand the dynamic controls of precipitation  
479 oxygen isotope ( $\delta^{18}\text{O}_p$ ). The IsoGSM2 has been widely used for both modern and past climate and isotope  
480 simulations and agrees well with available  $\delta^{18}\text{O}_p$  observations in the Global Network of Isotopes in  
481 Precipitation (GNIP) on annual and seasonal time scales. The IsoGSM2 model has been extensively  
482 validated for the Indian monsoon domain (29). IsoGSM2 has a horizontal resolution of ~200 km (T62)  
483 with 28 vertical levels. The model applies a global downscaling technique, which nudges temperature  
484 and wind speed (at scales larger than 1000 km) toward the National Center for Environmental

485 Prediction Reanalysis 2 (NCEP R2) (28,67). The nudging (performed at every 6 h for all sigma levels)  
486 provides dynamical constraints to the simulated atmospheric circulation and is directly comparable  
487 with the observations. In IsoGSM, most isotopic fractionations are assumed to occur at  
488 thermodynamic equilibrium, except for open water evaporation, condensation in supersaturation  
489 conditions (vapor to ice), raindrop re-evaporation, and air-rain isotopic exchange, where kinetic  
490 fractionation occurs. In the tracer mode, IsoGSM2 can track a given moisture mass back to its last  
491 time at sea level by setting the surface evaporative fractionation factor to 1 for the target region (and 0  
492 for all other regions) and by turning off all the other isotopic fractionation in the atmosphere. The  
493 evaporated water is marked by its origin with a tag. The tagged vapor once added to the atmosphere is  
494 allowed to undergo the same atmospheric hydrological cycle as normal water vapor until it leaves the  
495 atmosphere as precipitation (67). The tagged simulation output (1979 to 2010) was generated at daily  
496 intervals and interpolated into 17 vertical pressure levels and monthly averaged (67).  
497  
498

499 **ACKNOWLEDGEMENTS.** We thank A. S. Kathayat, G. Kathayat, N. Pant, S. Melkani, C. Dunnai, A.  
500 Dunnai, and the Meghalaya Adventurers Association led by B. K. Daly for their assistance during the fieldwork.  
501 **Funding:** We acknowledge support from the National Natural Science Foundation of China (NSFC) 41888101  
502 to (HC), and, 41703007, & 42172201 to (GK), and the Chinese Academy of Sciences (CAS) Presidents'  
503 International Fellowship Initiative (PIFI) grant 2020VCA0019 to AS.  
504

505 **Data Availability.** The data used in this study are reported in SI Appendix, Tables S1 and S2, or available at the  
506 National Oceanic and Atmospheric Administration (NOAA), [https://www.ncdc.noaa.gov/data-](https://www.ncdc.noaa.gov/data-access/paleoclimatology-data)  
507 [access/paleoclimatology-data](https://www.ncdc.noaa.gov/data-access/paleoclimatology-data)  
508

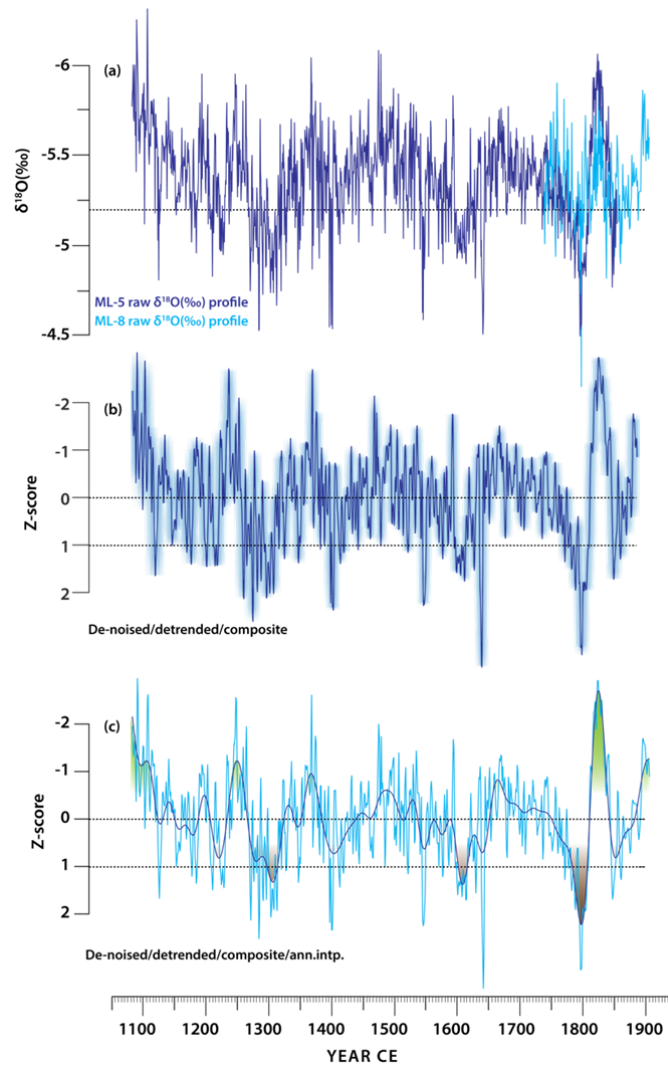
## 509 510 **References**

- 511  
512 1. S. Gadgil, S. Gadgil, The Indian Monsoon, GDP and Agriculture. *Economic and Political Weekly* 41,  
513 4887-4895 (2006).
- 514 2. B. Parthasarathy, A. A. Munot, D. R. Kothawale, All-India monthly and seasonal rainfall series:  
515 1871–1993. *Theoretical and Applied Climatology* 49, 217-224 (1994).
- 516 3. P. J. Webster, V. O. Magaña, T. N. Palmer, J. Shukla, R. A. Tomas, M. Yanai, T. Yasunari,  
517 Monsoons: Processes, predictability, and the prospects for prediction. *Journal of Geophysical*  
518 *Research: Oceans* 103, 14451-14510 (1998).
- 519 4. Indian Meteorological Department, <https://mausam.imd.gov.in/>.
- 520 5. D. Singh, R. Seager, B. I. Cook, M. Cane, M. Ting, E. Cook, M. Davis, Climate and the Global  
521 Famine of 1876–78. *Journal of Climate* 31, 9445-9467 (2018).
- 522 6. B.N. Goswami, The Asian monsoon: interdecadal variability. In *The Asian Monsoon*, Springer,  
523 Berlin, Heidelberg, 295-327 (2006).
- 524 7. M. K. Dhavalikar, in *Environment and Culture: A Historical Perspective* (Bhandarkar Oriental  
525 Research Institute, 2002).
- 526 8. A. Loveday, in *The history & economics of Indian famines.* (G. Bell and sons Limited, 1914).
- 527 9. G. Pant, K. Rupa Kumar, N. Sontakke, H. Borgaonkar, Climate variability over India on century and  
528 longer time scales. *Tropical Meteorology*, 149-158 (1993).
- 529 10. P. Whetton, I. Rutherford, Historical ENSO teleconnections in the Eastern Hemisphere. *Climatic*  
530 *Change* 28, 221-253 (1994).
- 531 11. R. H. Grove, J. Chappell, *El Niño, history and crisis: studies from the Asia-Pacific region* (White  
532 Horse Press, 2000).
- 533 12. G. C. Adamson, D. J. Nash, Documentary reconstruction of monsoon rainfall variability over western  
534 India, 1781–1860. *Climate Dynamics* 42, 749-769 (2014).
- 535 13. G. Thompson, T. Yao, E. Mosley-Thompson, M. Davis, K. Henderson, P.-N. Lin, A high-resolution  
536 millennial record of the South Asian monsoon from Himalayan ice cores. *Science* 289, 1916-1919  
537 (2000).
- 538 14. A. Sinha, K. G. Cannariato, L. D. Stott, H. Cheng, R. L. Edwards, M. G. Yadava, R. Ramesh, I. B.  
539 Singh, A 900-year (600 to 1500 AD) record of the Indian summer monsoon precipitation from the  
540 core monsoon zone of India. *Geophysical Research Letters* 34, GL030431 (2007).

- 541 15. A. Sinha, L. Stott, M. Berkelhammer, H. Cheng, R. L. Edwards, B. Buckley, M. Aldenderfer, M.  
542 Mudelsee, A global context for megadroughts in monsoon Asia during the past millennium.  
543 *Quaternary Science Reviews* 30, 47-62 (2011a).
- 544 16. A. Sinha, M. Berkelhammer, L. Stott, M. Mudelsee, H. Cheng, J. Biswas, The leading mode of Indian  
545 Summer Monsoon precipitation variability during the last millennium. *Geophysical Research Letters*  
546 38, GL047713 (2011b).
- 547 17. M. Berkelhammer, A. Sinha, M. Mudelsee, H. Cheng, R. L. Edwards, K. Cannariato, Persistent  
548 multidecadal power of the Indian Summer Monsoon. *Earth and Planetary Science Letters* 290, 166-  
549 172 (2010).
- 550 18. A. Sinha, G. Kathayat, H. Cheng, S. F. Breitenbach, M. Berkelhammer, M. Mudelsee, J. Biswas, R.  
551 Edwards, Trends and oscillations in the Indian summer monsoon rainfall over the last two millennia.  
552 *Nature Communications* 6, 1-8 (2015).
- 553 19. G. Kathayat, H. Cheng, A. Sinha, L. Yi, X. Li, H. Zhang, H. Li, Y. Ning, R. L. Edwards, The Indian  
554 monsoon variability and civilization changes in the Indian subcontinent. *Science Advances* 3,  
555 e1701296 (2017).
- 556 20. S. J. Burns, D. Fleitmann, M. Mudelsee, U. Neff, A. Matter, A. Mangini, A 780-year annually  
557 resolved record of Indian Ocean monsoon precipitation from a speleothem from south Oman. *Journal*  
558 *of Geophysical Research: Atmospheres* 107, ACL 9-1-ACL 9-9 (2002).
- 559 21. J. K. Wang, K. R. Johnson, A. Borsato, D. J. Amaya, M. L. Griffiths, G. M. Henderson, S. Frisia, A.  
560 Mason, Hydroclimatic variability in Southeast Asia over the past two millennia. *Earth and Planetary*  
561 *Science Letters* 525, 115737 (2019).
- 562 22. E. R. Cook, K. J. Anchukaitis, B. M. Buckley, R. D. D'Arrigo, G. C. Jacoby, W. E. Wright, Asian  
563 monsoon failure and megadrought during the last millennium. *Science* 328, 486-489 (2010).
- 564 23. S. Feng, Q. Hu, Q. Wu, M. E. Mann, A gridded reconstruction of warm season precipitation for Asia  
565 spanning the past half millennium. *Journal of Climate* 26, 2192-2204 (2013).
- 566 24. Shi, B. Wang, E. R. Cook, J. Liu, F. Liu, Asian summer precipitation over the past 544 years  
567 reconstructed by merging tree rings and historical documentary records. *Journal of Climate* 31, 7845-  
568 7861 (2018).
- 569 25. A. Levermann, J. Schewe, V. Petoukhov, H. Held, Basic mechanism for abrupt monsoon transitions.  
570 *Proceedings of the National Academy of Sciences* 106, 20572-20577 (2009).
- 571 26. S. F. Breitenbach, K. Rehfeld, B. Goswami, J. U. Baldini, H. E. Ridley, D. J. Kennett, K. M. Prufer,  
572 V. V. Aquino, Y. Asmerom, V. J. Polyak, Constructing proxy records from age models (COPRA).  
573 *Climate of the Past* 8, 1765-1779 (2012).
- 574 27. F. Murata, T. Terao, H. Fujinami, T. Hayashi, H. Asada, J. Matsumoto, H. J. Syiemlieh, Dominant  
575 synoptic disturbance in the extreme rainfall at Cherrapunji, Northeast India, based on 104 years of  
576 rainfall data (1902–2005). *Journal of Climate* 30, 8237-8251 (2017).
- 577 28. K. Yoshimura, M. Kanamitsu, D. Noone, T. Oki, Historical isotope simulation using reanalysis  
578 atmospheric data. *Journal of Geophysical Research: Atmospheres* 113, (2008).
- 579 29. G. Kathayat, A. Sinha, M. Tanoue, K. Yoshimura, H. Li, H. Zhang, H. Cheng, Interannual oxygen  
580 isotope variability in Indian summer monsoon precipitation reflects changes in moisture sources.  
581 *Communications Earth & Environment* 2, 1-10 (2021).
- 582 30. S. F. Breitenbach, J. F. Adkins, H. Meyer, N. Marwan, K. K. Kumar, G. H. Haug, Strong influence of  
583 water vapor source dynamics on stable isotopes in precipitation observed in Southern Meghalaya, NE  
584 India. *Earth and Planetary Science Letters* 292, 212-220 (2010).
- 585 31. M.P. Rao, E.R. Cook, B.I. Cook, R.D. D'Arrigo, F.G. Palmer, U. Lall, C.A. Woodhouse, B.M.  
586 Buckley, M. Uriarte, D.A. Bishop, J. Jian, Seven centuries of reconstructed Brahmaputra River  
587 discharge demonstrate underestimated high discharge and flood hazard frequency. *Nature*  
588 *Communications* 26, 1-0 (2020).
- 589 32. S. Dutt, A. K. Gupta, H. Cheng, S. C. Clemens, R. K. Singh, V. C. Tewari, Indian summer monsoon  
590 variability in northeastern India during the last two millennia. *Quaternary International* 571, 73-80  
591 (2021).
- 592 33. A.K. Gupta, S. Dutt, H. Cheng, R.K. Singh, Abrupt changes in Indian summer monsoon strength  
593 during the last~ 900 years and their linkages to socio-economic conditions in the Indian  
594 subcontinent. *Palaeogeography, Palaeoclimatology, Palaeoecology* 536, p.109347 (2019).

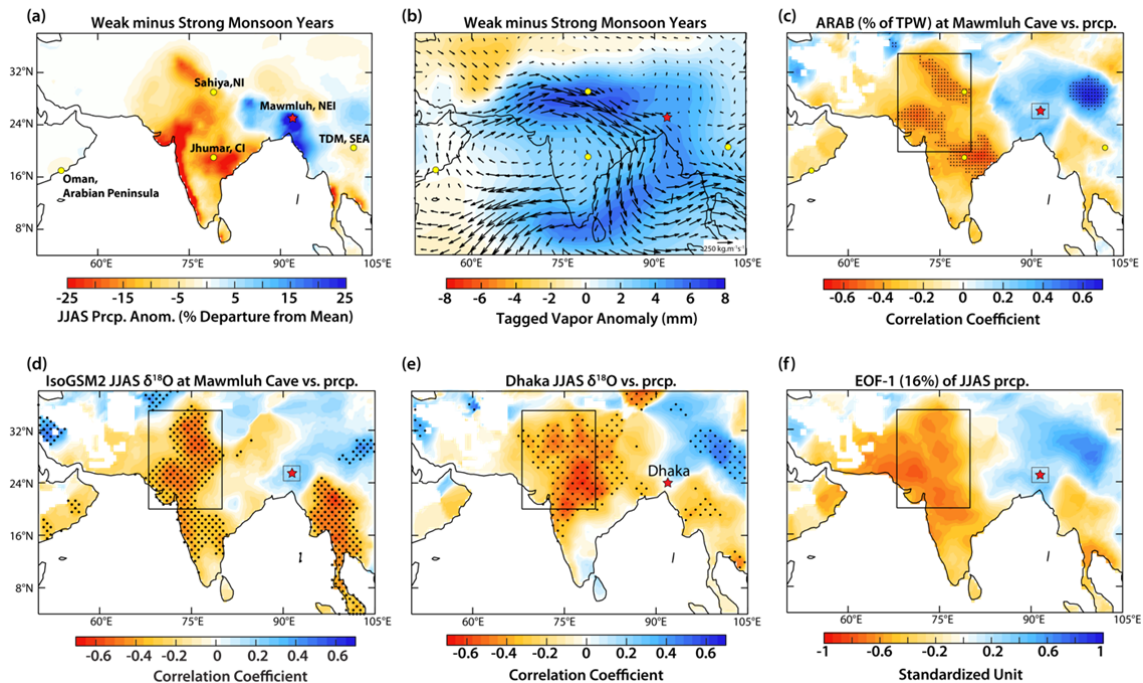
- 595 34. G. Myers, J. L. Oster, W. D. Sharp, R. Bennartz, N. P. Kelley, A. K. Covey, S. F. Breitenbach,  
596 Northeast Indian stalagmite records Pacific decadal climate change: Implications for moisture  
597 transport and drought in India. *Geophysical Research Letters* 42, 4124-4132 (2015).
- 598 35. R. E. Seavoy, *Famine in peasant societies* / Ronald E. Seavoy. Contributions in economics and  
599 economic history (Greenwood Press, New York, 1986) no. 66.
- 600 36. F. C. Danvers, *A Century of Famine*, Calcutta, (British Library India Office Records V/27/830/15) p.  
601 22 (1877).
- 602 37. V. Damodaran, R. Allan, A. E. Ogilvie, G. R. Demarée, J. Gergis, T. Mikami, A. Mikhail, S. E.  
603 Nicholson, S. Norrgård, J. Hamilton, in *The Palgrave handbook of climate history* (Springer, 2018),  
604 pp. 517-550.
- 605 38. D. Clingingsmith, J. G. Williamson, Deindustrialization in 18th and 19th century India: Mughal  
606 decline, climate shocks and British industrial ascent. *Explorations in Economic History* 45, 209-234  
607 (2008).
- 608 39. A. a.-F. I. ibn Mubārak, In *The Akbar Nāmā of Abu-l-Fazl*. (Printed at the Baptist Mission Press,  
609 1907), vol. 1.
- 610 40. P. Nath, Fatehpur Sikri revisited, by Syed Ali Nadeem Rezavi (Taylor & Francis, 2014) 389-393
- 611 41. S. K. Davar, The making of Fatehpur Sikri. *Journal of the Royal Society of Arts* 123, 781-805 (1975).
- 612 42. R. Grove, “El Nino Chronology and the History of Socio-economic and Agrarian Crisis in South and  
613 Southeast Asia 1250-1900” in *Land Use-Historical Perspectives: Focus on Indo-Gangetic Plains*, Y.P.  
614 Abrol, S. Sangwan, M. K. Tiwari, Eds (Allied Publishers, 2002).
- 615 43. M. Aldenderfer, Z. Yinong, The prehistory of the Tibetan Plateau to the seventh century AD:  
616 perspectives and research from China and the West since 1950. *Journal of World Prehistory* 18, 1-55  
617 (2004).
- 618 44. R. Vitali, in *The Kingdoms of Gu-ge Pu-hrang: According to MNga'-ris Rgyal-rabs* by Gu-ge Mkhan-  
619 chen Ngag-dbang Grags-pa. (Tho-ling gtsug-lag-khang lo-gcig-stong 'khor-ba'i rjes-dran-mdzag sgo'i  
620 go-sgrig tshogs-chung, 1996).
- 621 45. J. Han, Y. Yang, The socioeconomic effects of extreme drought events in northern China on the Ming  
622 dynasty in the late fifteenth century. *Climatic Change* 164, 1-17 (2021).
- 623 46. C. F. Ropelewski, M. S. Halpert, Global and regional scale precipitation patterns associated with the  
624 El Niño/Southern Oscillation. *Monthly Weather Review* 115, 1606-1626 (1987).
- 625 47. N. Saji, B. N. Goswami, P. Vinayachandran, T. Yamagata, A dipole mode in the tropical Indian  
626 Ocean. *Nature* 401, 360-363 (1999).
- 627 48. L. Krishnamurthy, V. Krishnamurthy, Influence of PDO on South Asian summer monsoon and  
628 monsoon-ENSO relation. *Climate Dynamics* 42, 2397-2410 (2014).
- 629 49. R. Krishnan, M. Sugi, Pacific decadal oscillation and variability of the Indian summer monsoon  
630 rainfall. *Climate Dynamics* 21, 233-242 (2003).
- 631 50. C. Torrence, P. J. Webster, Interdecadal changes in the ENSO-monsoon system. *Journal of Climate*  
632 12, 2679-2690 (1999).
- 633 51. K. K. Kumar, B. Rajagopalan, M. Hoerling, G. Bates, M. Cane, Unraveling the mystery of Indian  
634 monsoon failure during El Niño. *Science* 314, 115-119 (2006).
- 635 52. R. Garcia-Herrera, D. Barriopedro, E. Hernández, H. Diaz, R. Garcia, M. Prieto, R. Moyano, A  
636 chronology of El Nino events from primary documentary sources in northern Peru. *Journal of*  
637 *Climate* 21, 1948-1962 (2008).
- 638 53. J. L. Gergis, A. M. Fowler, A history of ENSO events since AD 1525: implications for future climate  
639 change. *Climatic Change* 92, 343-387 (2009).
- 640 54. Borah, V. Venugopal, J. Sukhatme, P. Muddebihal, B. Goswami, Indian monsoon derailed by a North  
641 Atlantic wavetrain. *Science* 370, 1335-1338 (2020).
- 642 55. Z. Wu, N. E. Huang, Ensemble empirical mode decomposition: a noise-assisted data analysis method.  
643 *Advances in Adaptive Data Analysis* 1, 1-41 (2009).
- 644 56. M. Ghil, M. Allen, M. Dettinger, K. Ide, D. Kondrashov, M. Mann, A. W. Robertson, A. Saunders, Y.  
645 Tian, F. Varadi, Advanced spectral methods for climatic time series. *Reviews of Geophysics* 40, 3-1-  
646 3-41 (2002).
- 647 57. I. Harris, P. Jones, CRU TS4. 01: Climatic Research Unit (CRU) Time-Series (TS) version 4.01 of  
648 high-resolution gridded data of month-by-month variation in climate (Jan. 1901–Dec. 2016). *Centre*  
649 *for Environmental Data Analysis* 25, (2017).

- 650 58. Y. Benjamini, Y. Hochberg, Controlling the False Discovery Rate: A Practical and Powerful  
651 Approach to Multiple Testing. *Journal of the Royal Statistical Society. Series B (Methodological)* 57,  
652 289-300 (1995).
- 653 59. S. F. Breitenbach, F. A. Lechleitner, H. Meyer, G. Diengdoh, D. Matthey, N. Marwan, Cave  
654 ventilation and rainfall signals in dripwater in a monsoonal setting—a monitoring study from NE India.  
655 *Chemical Geology* 402, 111-124 (2015).
- 656 60. R. L. Edwards, F. W. Taylor, J. Chen, G. Wasserburg, High Precision Thorium-230 Dating of Corals  
657 Using Thermal Ionization Mass Spectrometry: Applications to Paleoseismology. University of Texas  
658 Institute for Geophysics Technical Reports, (1987).
- 659 61. H. Cheng, R. L. Edwards, C.-C. Shen, V. J. Polyak, Y. Asmerom, J. Woodhead, J. Hellstrom, Y.  
660 Wang, X. Kong, C. Spötl, Improvements in <sup>230</sup>Th dating, <sup>230</sup>Th and <sup>234</sup>U half-life values, and U–Th  
661 isotopic measurements by multi-collector inductively coupled plasma mass spectrometry. *Earth and  
662 Planetary Science Letters* 371, 82-91 (2013).
- 663 62. D. J. Thomson, Spectrum estimation and harmonic analysis. *Proceedings of the IEEE* 70, 1055-1096  
664 (1982).
- 665 63. A. Springford, G. M. Eadie, D. J. Thomson, Improving the lomb–scargle periodogram with the  
666 thomson multitaper. *The Astronomical Journal* 159, 205 (2020).
- 667 64. C. Torrence, G. P. Compo, A practical guide to wavelet analysis. *Bulletin of the American  
668 Meteorological Society* 79, 61-78 (1998).
- 669 65. Gerber M. E. FDR (False Discovery Rate) ([https://www.mathworks.com/  
670 matlabcentral/fileexchange/71734-fdr-false-discovery-rate](https://www.mathworks.com/matlabcentral/fileexchange/71734-fdr-false-discovery-rate)), MATLAB Central File Exchange.  
671 Retrieved February 17, (2021).
- 672 66. K. Yoshimura, M. Kanamitsu, Dynamical global downscaling of global reanalysis. *Monthly Weather  
673 Review* 136, 2983-2998 (2008).
- 674 67. M. Tanoue, K. Ichianagi, K. Yoshimura, M. Kiguchi, T. Terao, T. Hayashi, Seasonal variation in  
675 isotopic composition and the origin of precipitation over Bangladesh. *Progress in Earth and  
676 Planetary Science* 5(1), 1-6. (2018).
- 677



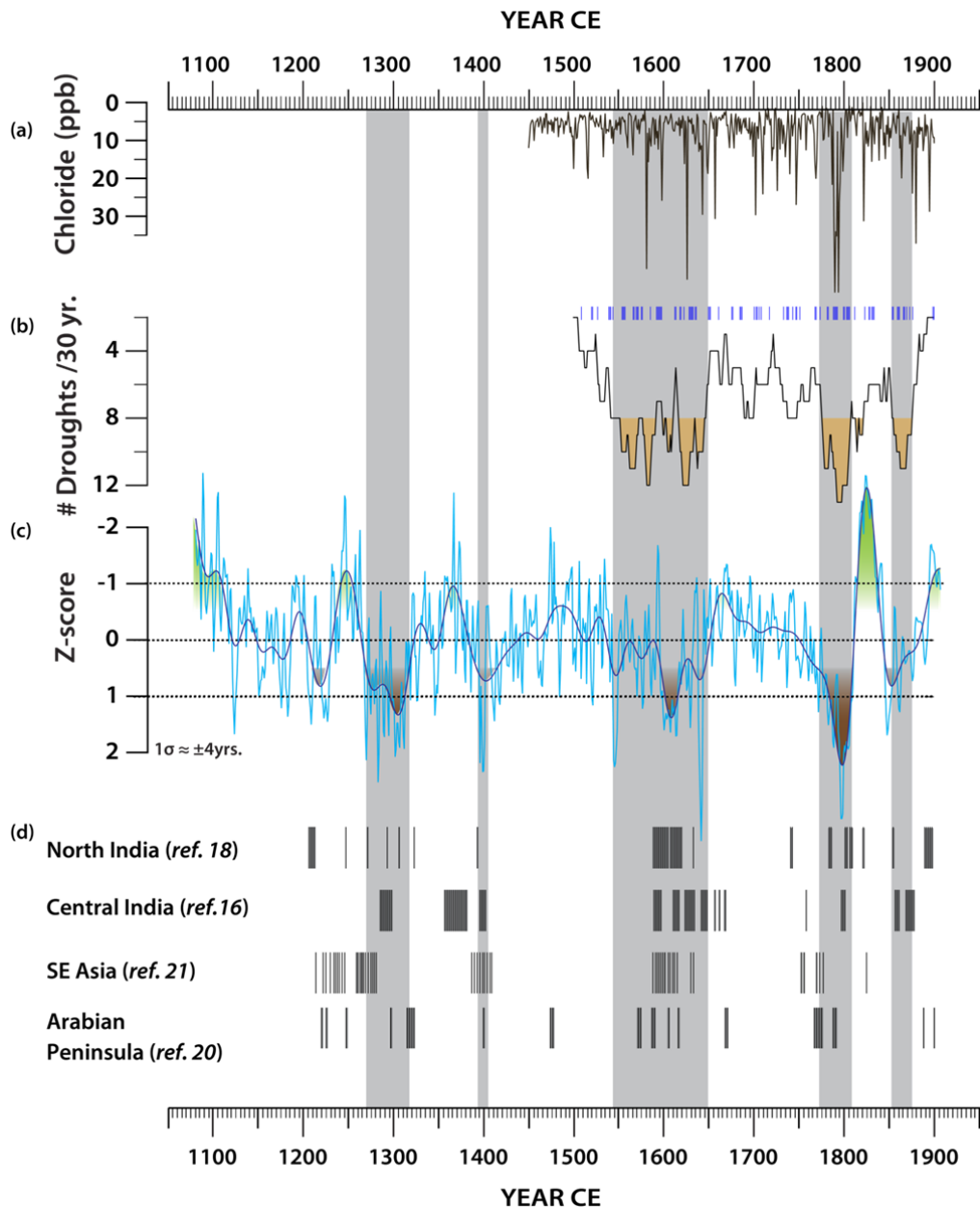
678  
 679  
 680  
 681  
 682  
 683  
 684  
 685  
 686  
 687  
 688  
 689  
 690  
 691  
 692

**Figure 1. Mawmluh cave speleothem  $\delta^{18}\text{O}$  records.** (a) Raw  $\delta^{18}\text{O}$  profiles of ML-5 (indigo) and ML-8 (cyan) on their independent age models. The mean  $\delta^{18}\text{O}$  value is indicated by a horizontal dotted line. The ML-5 and ML-8  $\delta^{18}\text{O}$  profiles were subsequently combined by stacking on a common age scale (see [SI Appendix, Fig. S4, Materials and Methods](#)). (b) The de-noised, detrended, and z-score transformed MAW profile (indigo) is shown along with the  $1\sigma$  age uncertainty based on the Monte Carlo results from COPRA (shaded) (26) ([Materials and Methods](#)). The median age was selected as the final age model ([SI Appendix, Fig. S3, Materials and Methods](#)). The high-frequency ( $\sim 1$ -2 years) noise and long-term ( $>200$  years) non-linear trends were removed by using the ensemble empirical mode decomposition (55) and singular spectrum analysis (56) ([SI Appendix, Fig. S5, Materials and Methods](#)). (c) Annually interpolated MAW profile (from b) on its median age (cyan) overlain by a 30-year lowpass Butterworth filter (indigo). Shades of brown and green delineate multidecadal periods of inferred droughts ( $z\text{-score} > 1$ ) and pluvial conditions ( $z\text{-score} < -1$ ).



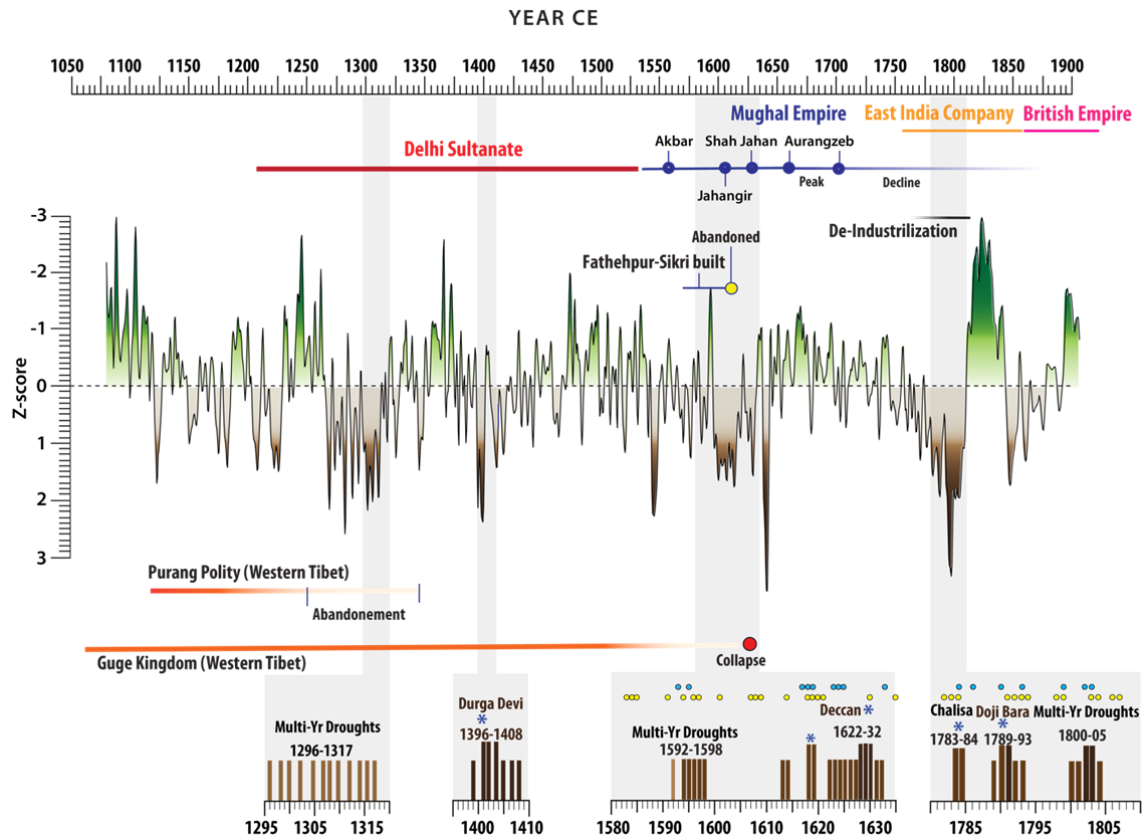
693  
694  
695  
696  
697  
698  
699  
700  
701  
702  
703  
704  
705  
706  
707  
708  
709  
710  
711  
712  
713  
714  
715  
716  
717  
718  
719

**Figure 2. Spatial patterns of climate field anomalies and proxy locations.** (a-b) Spatial patterns of JJAS anomalies (weak monsoon minus strong monsoon years) from the monthly Climatic Research Unit (CRU) TS4.03 (57) and tagged Arabian Sea moisture (ARAB) anomalies are shown as fractions of total precipitable water (% TPW, shaded, from ref. 29) overlain by the vertically integrated moisture flux anomalies (black arrows) (28). (c) The inverse field correlations between the JJAS ARAB (% TPW) extracted from the grid points nearest to Mawmluh cave (small square) and precipitation amount at all other grid points (58). Note that the increased flux of  $^{18}\text{O}$ -enriched ARAB moisture over NEI India is associated with reduced rainfall over the rest of the Indian subcontinent. (d) Same as panel c, but for simulated JJAS precipitation oxygen isotope ( $\delta^{18}\text{O}_p$ ) data extracted from the grid points nearest to Mawmluh cave (28) and precipitation amount (57). Note that the higher (lower)  $\delta^{18}\text{O}$  values over NEI are associated with reduced (increased) rainfall over the rest of the Indian subcontinent. (e) Same as panel d but for spatial correlations between the observed amount weighted JJAS  $\delta^{18}\text{O}_p$  at Dhaka and the precipitation amount at other grid points for the period from 2009-2016 (see ref. 29 for details). (f) The first Empirical Orthogonal Function (EOF) mode of normalized JJAS precipitation (57) over the region  $38^\circ\text{N}$  to  $4^\circ\text{S}$  and  $50^\circ\text{W}$  to  $105^\circ\text{E}$ . The EOF-1 (explained variance  $\sim 16\%$ ) shows a precipitation dipole akin to the observed weak minus strong pattern of JJAS rainfall anomalies as in panel a. The locations of Mawmluh cave (red star), other cave records (yellow dots), and Dhaka (yellow star) are shown in different panels. Stippling on panels (c-e) indicates regions of significant correlations at the 95% significance level obtained after accounting for serial correlations in data at each grid point followed by the application of the False Discovery Rate (FDR) procedure (58) with a 5% threshold (*Materials and Methods*). FDR is the expected proportion of rejected hypotheses when the null hypothesis is true for those tests. Large black rectangles ( $\sim 20^\circ\text{N}$ - $35^\circ\text{N}$ ;  $68^\circ\text{E}$ - $80^\circ\text{E}$  and small squares  $\sim 27^\circ\text{N}$ - $23^\circ\text{N}$ ;  $90^\circ\text{E}$ - $94^\circ\text{E}$ ) in panels c-f demarcate the region where the JJAS precipitation amount is strongly and inversely correlated to the model-derived  $\delta^{18}\text{O}_p$  and tagged ARAB (% TPW) extracted from the grid cell nearest to Mawmluh cave. These timeseries comparisons are shown in *SI Appendix, Figure S6*.



720  
721  
722  
723  
724  
725  
726  
727  
728  
729  
730  
731  
732

**Figure 3. Comparison of the MAW record with historic data and other proxy records. (a)** The chloride concentrations in Dasuopu ice core, Himalaya (red) (13). **(b)** Historic drought frequency in a 30-year moving average (black) (11). The drought frequency >8 is highlighted (shaded). **Historic drought years are shown by vertical blue lines.** **(c)** MAW  $\delta^{18}O$  record (this study, cyan) overlain a 30-year Butterworth low-pass filter (indigo). The dotted black line highlights the z-score values delineating several multidecadal periods of inferred droughts (z-score >1). **(d)** Vertical black lines show extreme dry events derived from the de-noised, detrended, annually interpolated speleothem  $\delta^{18}O$  records (based on z-score thresholds > 90 % percentile  $\sim >1.25$ ) in each of the following records: Sahiya cave (30°36'N, 77°52'E) (18), North India; Jhumar/Dandak cave (18°52'N, 81°52'E) (15, 16), central India; Tham Doun Mai cave (20°45'N, 102°39'E) (21), Laos, Southeast Asia; and Oman cave (17°10'N, 54°18'E) (20), Arabian Peninsula (also see *SI Appendix, Fig. S9* for a detailed comparison). The vertical bars (shaded) highlight intervals of multi-year droughts identified in the MAW record and historical drought compilations.



733  
734  
735  
736  
737  
738  
739  
740  
741  
742  
743

**Figure 4. The MAW record, geopolitical context, and historic droughts.** The interpolated MAW record (0.6 years, black) with multidecadal periods of inferred droughts (z-score >1, brown) and pluvial conditions (z-score <-1, green). The insets show historic droughts (light and dark brown bars) over the Indian subcontinent (11) (*SI Appendix, Text S1*). The historic droughts reported with high reliability are shown by the dark brown bars. The catastrophic droughts and famines associated with mass mortality events are shown by the asterisks (also see *SI Appendix, Fig. S10*). Historic El Niño events are shown with yellow (52) and cyan (53) circles. The text associated with solid and varying saturation intensity-colored lines describes the various political/dynastic timelines and key events discussed in the *SI Appendix, Text S1*.

